Journal of Power Sources 450 (2020) 227595

Contents lists available at ScienceDirect

Journal of Power Sources

journal homepage: www.elsevier.com/locate/jpowsour

Effect of binder on the overcharge response in $LiFePO_4$-containing cells

Nancy Dietz Rago [a], Jianlin Li [b,*], Yangping Sheng [b], David L. Wood III [b], Leigh Anna Steele [c], Joshua Lamb [c], Christopher Grosso [c], Kyle Fenton [c], Ira Bloom [a,**]

[a] Chemical Sciences and Engineering Division, Argonne National Laboratory, Lemont, IL, 60439, USA
[b] Energy and Transportation Science Division, Oak Ridge National Laboratory, Oak Ridge, TN, 37831, USA
[c] Power Sources Technology Group, Sandia National Laboratories, Albuquerque, NM, 87185, USA

HIGHLIGHTS

- LFP/Graphite cells made with pVdF or CMC binders were overcharged to 100–250% SOC.
- Marked microstructural changes in the anode with SOC were seen in those with CMC.
- The number of organics in the SEI was sensitive to binder.

ARTICLE INFO

Keywords:
Lithium-ion battery
Overcharge
Binders
$LiFePO_4$

ABSTRACT

Two types of small pouch cells based on $LiFePO_4$/graphite, one containing a N-methyl pyrrolidinone (NMP)-soluble binder, poly(vinylidene difluoride), and the other an aqueous-soluble binder, styrene-butadiene rubber/carboxymethylcellulose were systematically charged to 100, 120, 140, 160, 180, and 250% state of charge (SOC). The cells were then discharged to 3.0 V at room temperature before being disassembled for postmortem analysis. Microstructural changes in the anode associated with increasing SOC were more pronounced in the aqueous processed cells in comparison to the NMP-processed cells. Dendrite formation was observed on the aqueous-processed anode at 120% SOC, while the NMP-processed anode surface does not show dendrites until 250% SOC. Overall, the aqueous-processed anode surfaces displayed more evidence of microstructural degradation as a function of increasing SOC. In the NMP-processed cells, four organic compounds on the anode surface were found to show a dependence on SOC, while only two displayed a similar dependency in the aqueous-processed cells. The nature of the binder changed the number and composition of the species found at the anode.

1. Introduction

Lithium ion cells and batteries are becoming ubiquitous in many applications, such as in consumer electronics and in transportation. This is due to their very attractive combination of high specific power and energy. In general terms, these cells consist of a lithiated metal oxide or phosphate positive electrode, an electrolyte consisting of one or more lithium salts dissolved in mixed organic carbonates, and a graphite negative electrode. With the wide acceptance of these cells, questions of safety are paramount. That is, how does the battery respond to what might be termed abusive conditions, such as over temperature and overcharging? Understanding the chemical basis of the overcharge response should provide useful information from a battery safety perspective.

There are, in theory, many ways to engineer overcharge tolerance into a lithium-ion cell. For example, Odom et al. showed how N-substituted phenothiazines formed redox shuttles in $LiFePO_4$ (LFP)/graphite cells [1]. Another example is the use of electro-active polymers in the separator, such as that used by Wang et al. [2]. Yet another strategy is to use CuO as an additive in $LiCoO_2$ and $LiMn_2O_4$ cathodes, which could be cycled to 5 V versus Li/Li^+. Here, the authors hypothesize that CuO decomposed to Cu^{2+} (and oxygen gas), which was reduced to Cu^+ at the anode. The dissolved copper ions form a redox shuttle in the cycling cell [3]. Thus, an understanding of the fundamental changes, which occur during overcharge, may help mitigate the response of the cell.

In earlier publications, Argonne National Laboratory (Argonne), Oak Ridge National Laboratory (ORNL), and Sandia National Laboratories

* Corresponding author.
** Corresponding author.
E-mail addresses: lij4@ornl.gov (J. Li), ira.bloom@anl.gov (I. Bloom).

https://doi.org/10.1016/j.jpowsour.2019.227595
Received 25 September 2019; Received in revised form 15 November 2019; Accepted 8 December 2019
Available online 29 January 2020

presented their results from systematic studies of the overcharge response of cells containing $Li(Ni_{0.5}Mn_{0.3}Co_{0.2})O_2$ (NMC532) cathodes, an electrolyte consisting of 1.2 M $LiPF_6$ in ethylene carbonate:diethylcarbonate (EC:DEC) (3:7 by weight) and graphite anodes. Here, poly (vinylene difluoride) (pVdF) binders were in both electrodes. A series of papers [4–6] showed the basic changes in the chemistry and morphology of the electrodes and solid electrolyte interphase (SEI) layer in these cells and how the changes responded to different states of charge, such as 100, 120, 140, 160, 180, and 250%. These papers served as the basis of comparison for other related work, such as the impact of binder on abuse response.

Some information regarding the overcharge response of LFP-containing cell is available in the open literature [7–11]. These reports focused on the thermal runaway characteristics of highly charged LFP-containing cells but did not provide detailed analyses of the physical and chemical changes that occurred in the overcharged cells.

Xu et al. [9] reported results from LFP cells that were overcharged by 5–20% (105–120% state of charge [SOC]). They characterized the changes that occurred using scanning electron microscopy (SEM)/energy-dispersive spectroscopy, high-energy X-ray diffraction and cyclic voltammetry. They provided detailed analysis on a cell that was overcharged by 10% (110% SOC), showing that iron deposits most likely bridged the separator.

Liu et al. [11] investigated the effect of cycling 18,650-sized cells to 110% SOC. Their results showed that electrochemical impedance spectroscopy could be used to monitor the state of health of the cells. With continued cycling, the capacity of the cells decreased markedly. Their electrochemical impedance spectroscopy results showed rapid increases in ohmic, charge-transfer, and Warburg impedances after about 10 cycles.

All reports focused on the overcharge response of a given cell. There were none that provided a systematic investigation. Additionally, there were no reports describing the effect of changing what seems to be an innocuous component of the cell, the binder, on overcharge response. The lack of these results, in part, provided motivation for our study.

In this study, cells were charged to 100, 120, 140, 160, 180, and 250% SOC and subsequently discharged to 0% SOC before being subjected to post-test analysis. After disassembly in an argon-filled glove box, sections of the electrodes were prepared for detailed characterization. We characterized the changes in surface morphology and chemical changes in the negative electrode. In this paper, we describe our results from SEM and HPLC as they relate to information regarding changes in surface morphology and chemical changes in the bulk anode and materials on its surface.

2. Experimental

Most of the experimental materials and procedures have already been described [4–6]. They are provided below for the reader's convenience.

2.1. Materials

Lithium-ion 1.2-Ah cells containing $LiFePO_4$/graphite chemistry were fabricated and formed as described below. The 1.2-Ah capacity rating represented 95+% of the theoretical amount of lithium in the cathode material.

The LFP cathode was coated on an Al foil, which was treated by corona treatment (4.4 J cm^{-2}) for superior slurry wetting on the substrate [12] for the aqueous processed one following similar electrode fabrication reported in a previous publication [13]. The negative-to-positive ratio was 1.1:1. Except for the outer two layers, all electrodes were double-sided. The compositions of the two types of electrodes are given in Table 1a and 1b.

The electrodes went through a secondary drying at 100 °C under vacuum overnight before being assembled into pouch cells in a dry room with a relative humidity below 0.1%. In both cases, the separator consisted of a polypropylene–polyethylene–polypropylene trilayer (Celgard® 2325; 89 mm × 61 mm × 25 μm). The electrolyte consisted of 1.2 M $LiPF_6$ in EC:DEC (3:7 by weight, BASF).

Table 1a
Cell construction information using the NMP-soluble binder.

Electrode	Composition	Electrode size (loading)
Negative	92 wt% A12 graphite (ConocoPhillips), 2 wt% C-65 carbon black (Timcal), 6 wt% 9300 pVdF (Kureha 9300) 35% porosity	86.4 mm × 58 mm (4.52 mg cm^{-2})
Positive	85 wt% $LiFePO_4$ (BASF, 3.6 wt% carbon), 7.5 wt% C-65 carbon black (Timcal), 7.5 wt% 5130 pVdF (Solvay) 40% porosity	84.4 mm × 56 mm (8.22 mg cm^{-2})

Table 1b
Cell construction information using the aqueous binder.

Electrode	Composition	Electrode size (loading)
Negative	92 wt% A12 graphite (ConocoPhillips), 2 wt% C-65 carbon black (Timcal), 4.8 wt% SBR (Targrey)/1.2 wt% carboxymethylcellulose (CMC) (Sigma Aldrich, M_w = 250, 000; DS = 0.9) 35% porosity	86.4 mm × 58 mm (4.44 mg cm^{-2})
Positive	85 wt% $LiFePO_4$ (BASF, 3.6 wt% carbon), 7.5 wt % C-65 carbon black (Timcal), 5.25 wt% pVdF Latex (Solvay Solef® XPH-859)/2.25 wt% CMC (Sigma Aldrich, M_w = 250, 000; DS = 0.9) 40% porosity	84.4 mm × 56 mm (8.38 mg cm^{-2})

The pouch cells were tap-charged at C/10 for 15 min, rested for 6 h, and went through 4 charge-discharge cycles at C/20 between 2.5 and 4.2 V for formation cycles. After formation, the cells were shipped to Sandia National Laboratories for overcharging. They were charged to 100, 120, 140, 160, 180, and 250% SOC, as described in a previous publication [4].[1]

2.2. SEM

In an argon-filled glove box, the cells were opened using ceramic scissors. The electrodes were removed from the separator and allowed to dry. Sections of the anodes were cleaned two times by swirling 1 min each in excess dimethylcarbonate.

Pieces of electrode samples were placed in an airtight holder, based on the design published by ORNL [14]. After mounting the sample, the sealed holder was removed from the glove box and evacuated. After evacuation, the lid screws were removed, and the holder was placed in a JEOL JSM-6610LV scanning electron microscope. In the SEM column, the holder lid opened when the vacuum in the column exceeded the vacuum inside the holder. Energy-dispersive spectroscopy was performed using an Oxford Instruments $XMax^N$ detector (detector size = 50 mm^2) and AZtecEnergy® software.

2.3. HPLC

Samples for HPLC analysis were prepared by scraping the anode coating (~100 mg) off the copper foil from the cells. The scrapings were placed in scintillation vials, then covered and removed from the glove box. Approximately 1–1.5 mL of HPLC-grade water (Sigma-Aldrich) and ~20–30 mg reagent-grade Na_2CO_3 were added to each vial. Sodium carbonate was used to neutralize any nascent HF that formed during this step.

[1] *%SOC = 100% + %(rated capacity) added. The amount of capacity added was determined by monitoring the current for a fixed period (coulomb counting).*

In some cases, a small number of bubbles formed, indicating the presence of residual lithium. The contents of each vial were mixed thoroughly using a vortex mixer after the bubbling (if any) stopped. Approximately 2–2.5 mL CH_2Cl_2 (Sigma-Aldrich; Chromasolv®) was added to each vial. Again, the contents of each vial were blended thoroughly using the vortex mixer. After the layers separated, the solids tended to stay in the upper, aqueous layer and the bottom, organic layer was carefully removed using a pipette, placed in another scintillation vial, and allowed to dry overnight. The residue was then taken up in ~0.5 mL acetonitrile (HPLC grade), placed in an amber HPLC vial, and capped. The sample vials were placed in the autosampler.

HPLC analyses were performed using an Agilent Technologies 1260 Infinity chromatograph equipped with an auto-sampler (Agilent Technologies G1329B); a quaternary pump (Agilent Technologies G1311B); and an electrospray, quadrupole mass spectrometer detector (MSD; Agilent Technologies 6120). The fragmenting voltage in the MSD was 70 V and data were collected in the range of 50–1000 Da. Separations were performed using a Zorbax® ODS column (5 μm, 4.6 × 250 mm), which was thermostated at 25 °C. Water and acetonitrile (both HPLC-grade, Sigma-Aldrich, and containing 0.1% formic acid) were mixed in a 60/40 v/v ratio using the quaternary pump to form the mobile phase. The pumping speed was 1 mL min^{-1}. The column was purged with the mobile phase for 5–10 min before use.

2.4. HPLC data reduction and calculations

The data in a selected region were used to construct single-ion chromatograms. A tolerance band of −0.7 to +0.3 Da around the selected values was used. The data were categorized in terms of mass and total abundance; the computer-based method for this is given below in pseudocode:

```
Create table indexed on mass
Find start and end times to define selected region
For each mass in region
   Is mass in the mass table?
      Yes: add abundance to current abundance value for
      the given mass
      No: add mass and abundance to table
Create list of (mass, abundance) pairs
Sort list on abundance (maximum to minimum)
Read top 15 most-abundant masses from sorted list
   Create abundance vs. time profiles for the masses
   from the original data from most-abundant masses
```

The mass spectra were calculated from these abundance versus time profiles and the raw MSD data using some of the principles described by Malinowski [15]. The mathematics are described in more detail in a previous work [5].

Pearson's *r* was used as an aid to determine which peaks correlated with a selected one. The formula for Pearson's *r* is shown in Eq. (1) [16] and was used as an aid to determine the molecular ion peak. If a group of single-ion chromatograms had high values of *r* (~0.90 or higher), they were considered to be correlated and from the same molecule. The retention time plots of the correlated ions were used as confirmation:

$$\frac{r=\sum(x-\bar{x})(y-\bar{y})}{\sqrt{\sum(x-\bar{x})^2\sum(y-\bar{y})^2}} \quad \text{(Eq. 1)}$$

3. Results

After storage at room temperature, the capacities of the cells were in the range of about 0.9–1.2 Ah. In this paper, percent SOC is based upon rated capacity. Fig. 1 provides the cell voltage versus percent SOC during charging.

Once past 100% SOC, all electrochemically active lithium has been consumed. The cell polarizes with increasing SOC, until, at about 120% SOC, the polarization stops at 5.9 V. It appears that, in the range of ~120% to ~135–140% SOC, the current is carried by some other process, such as the oxidation of the carbon in the cathode or of the electrolyte near the cathode. At states of charge beyond 140% SOC, another process seems to be active, preventing the cell from reaching the 20-V potential of the power supply.

For the NMP-processed cells, only the 100% SOC cells did not appear inflated. The 120–160% SOC cells were inflated and the 180 and 250% SOC cells vented. The fact that the cells inflated implied that gas was generated, which is indicative of electrolyte oxidation. The electrolyte in the porous electrode structure would then be pushed out, resulting in oddly shaped voltage response curves.

3.1. Initial disassembly

Based on visual inspection of the anode surfaces during disassembly, the aqueous processed anode surfaces appear to be reacting more aggressively based on the degree of surface discoloration. Because this discoloration is associated with microstructural changes, a correlation can be made between degradation during overcharge and local inhomogeneities across the laminate surface. Nonuniform discoloration of the anode surfaces and corresponding separators occurred with increasing SOC in both NMP- and aqueous-processed cells; however, the nature of the discoloration was different. Fig. 2 shows glove box images of the aqueous and NMP-processed anode surfaces. The aqueous processed anode surfaces had a spotted pattern, whereas the NMP-processed anode surface did not show much discernible discoloration until 180% SOC, and the discoloration was more of a marbled pattern without the distinct spots seen in the aqueous process anode and separator. Even after rinsing in DMC, which presumably removed precipitated salts and soluble reaction products, most of the discoloration on the anode's surfaces remained. Both anode surfaces showed some degree of pull-out of the active material onto the separator during disassembly. The spotted pattern of discoloration in the aqueous processed anode surface could be, to some extent, remaining aggregates of the surface material that was pulled out onto the separator. SEM observation confirmed the existence of surface aggregates, but they did not appear to be present in the same frequency as they are in the optical images. In addition to the aggregates, splotchy dark regions were also present.

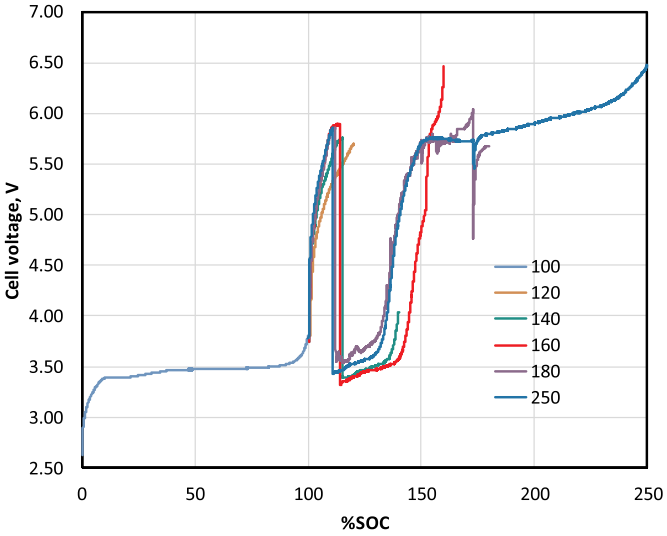

Fig. 1. Cell voltage vs. %SOC during charging for NMP-processed cells. Capacity data were recast as %SOC to facilitate graphical comparison. The 100% SOC curve is implicit in the others. The voltage vs. %SOC curves for the aqueous-processed cells were analogous.

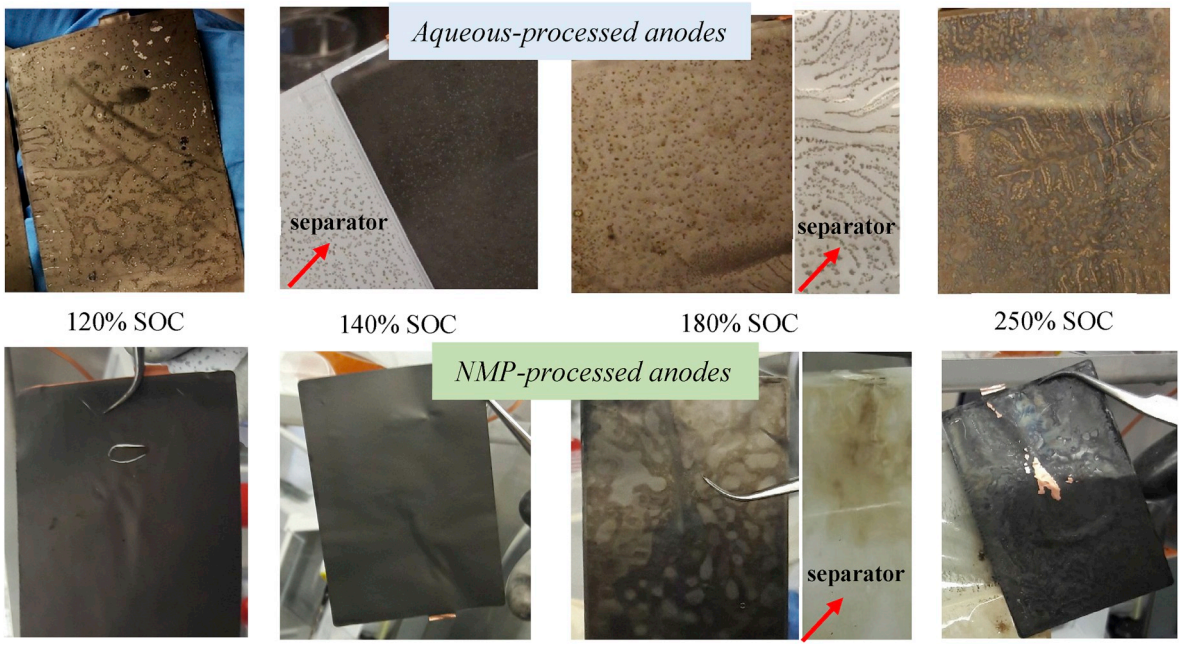

Fig. 2. Glove box images of aqueous and NMP-processed anodes upon disassembly. Arrows point to separators for the indicated anode.

Some of the anodes in the NMP-processed cells had areas that appeared buckled, indicating a possible breakdown of binder adhesion to the collector.

The change in microstructural features with increasing SOC could be due to areas that have become electrically disconnected from the collector, variation in current density, or nonuniform distribution of electrolyte/reaction products.

3.2. SEM

In the present paper, only the salient differences between the aqueous-processed and NMP-processed cells are discussed, highlighting the most demonstrative SOC in terms of microstructural changes.

Fig. 3 shows the surfaces of the 120, 140, 180, and 250% SOC anodes. Surface aggregates are present throughout all SOCs on the aqueous processed anodes. In contrast, the NMP-processed anode surfaces appear relatively unreacted until 180% SOC, at which point splotchy discoloration is apparent; this discoloration becomes even more pronounced at 250% SOC.

All SOCs on the aqueous processed anodes had isolated areas of the SEI in addition to surface aggregates that consist of packed dendrites. Graphite particles could be seen in the remaining areas, often covered with small submicron particles. Most of the SEI regions appear as pools of amorphous cracked material, while some regions had only a barely noticeable thin veil of SEI coverage. The aggregates and the SEI regions were relatively high in F, and the dendrite aggregates contained the highest concentration of F and P. A sparse distribution of discrete Fe particles was detected on the 100 and 120% SOC anode surfaces. At 120% SOC, some of these Fe particles were associated with Cr and Ni, indicating possible contamination from stainless steel. Previous studies concluded that this contamination came from the starting materials in the production of LFP and that it was responsible for dendrite formation

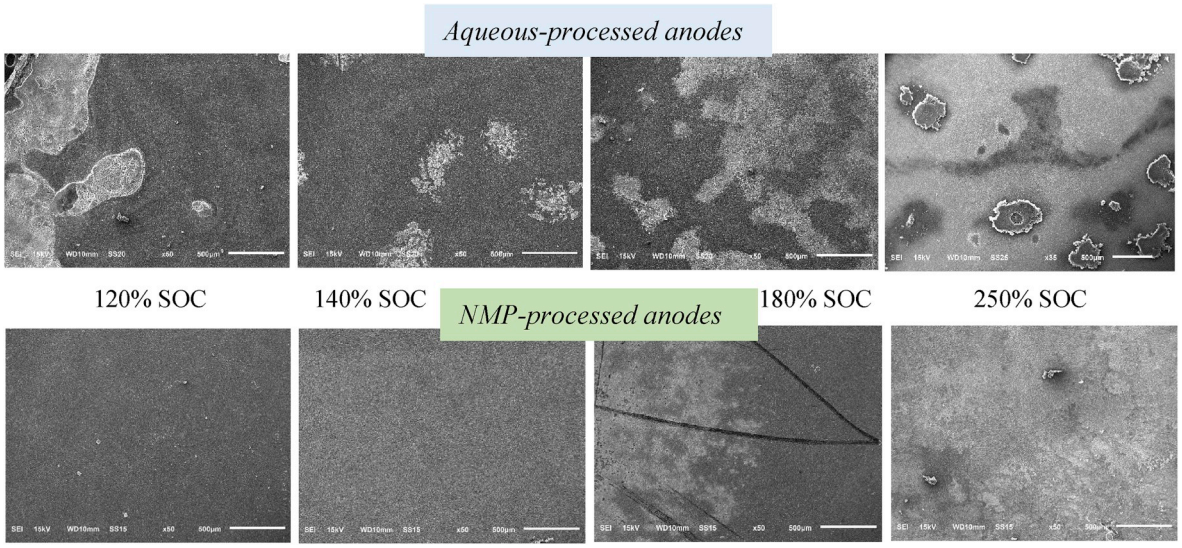

Fig. 3. Aqueous- and NMP-processed anode surfaces at the same magnification showing surface aggregates on the aqueous-processed anode surfaces in comparison to the relatively unreacted surfaces of the NMP-processed anodes.

that ultimately led to cell failure [9].

Fig. 4 shows the evolution of microstructural features with increasing SOC. At 120% SOC, the aqueous processed anode surface shows the beginning of dendrite formation through the SEI. This is not visible in the NMP-processed anode surface until 250% SOC, a significant delay in the nucleation of dendrites. At 140 and 160% SOC, Fe was always associated with the observable SEI layer and was not seen as discrete particles but part of the SEI layer. At 180 and 250% SOC, Fe was not detected. Trace Na was detected on the surface of all the aqueous processed anodes, which was from the CMC binder.

By 180% SOC, the aqueous processed anode surface had more dendrite coverage and regions of graphite particles covered with nanoscale particles that appeared to be in a thin film, presumably a thin SEI layer. At 250% SOC, the graphite particles were completely coated with submicron particles that were covered, in turn, with nanoscale particles. The dendrites were heavily coated as well.

In comparison to the aqueous processed anode surfaces, the NMP-processed anode surface microstructure consisted mainly of graphite particles that became progressively covered with particles with increasing percent SOC. These particles could be associated with an SEI layer, although an obvious SEI was not observed until 250% SOC. At 250% SOC, there appear to be areas of the SEI layer that are turning into structures like those seen at the beginning of dendrite growth. These areas were associated with the highest amounts of F. Most of the surface at 250% SOC is covered with an SEI layer. In general, F increased with increasing SOC, but concentrations were considerably lower in comparison to F concentration on the aqueous-processed anode surface. However, the dendrites in the 250% SOC NMP-processed anode had very high concentrations of F, around 40 at%.

In our previous overcharge study using NMC532 instead of LFP [4], the cathode surfaces were unremarkable. In this study, there is a distinct difference between the cathode surfaces with increasing SOC. Fig. 5 shows the aqueous- and NMP-processed cathode surfaces at 250% SOC. The aqueous-processed cathode surface is covered with small round flat particles that are coalesced in some areas. The NMP-processed cathode surface is covered in an amorphous film, or cathode electrolyte interphase layer, that gradually encroaches on the surface with increasing SOC.

3.3. HPLC

This section will be divided into the general approach taken to interpret the HPLC data, the results from the NMP-processed cells, and those from the aqueous-processed cells. This was done to facilitate comprehension. Plots of total ion count from the MSD versus time are given in the Supplemental Material in Figs. S1 and S2, respectively, for the NMP- and aqueous-processed materials. Note that the HPLC data from the 250% SOC NMP-processed samples did not yield compounds that followed an SOC-dependent trend. These data are shown in the Appendix also, but were omitted from the discussion below for the sake of clarity.

3.3.1. General approach

Single-ion chromatograms were constructed using, for example, the data shown in Fig. S2. The data were examined systematically, looking for a peak that aligned with a peak in the total ion chromatogram. An example of this is shown in Fig. 6 for m/e = 315 and some of the data from 160% SOC cell containing aqueous-processed materials.

The corresponding mass spectrum was calculated using the methods outlined by Malinowski et al. [15]. It was assumed that the compounds that produced the mass spectra were organic and should, therefore, have peaks that correspond to ^{12}C and ^{13}C incorporation at m and (m+1). Pearson's r was used to facilitate the selection of these peaks. If the value of Pearson's r was ~0.9 or greater, the peaks were assumed to be correlated and from the same compound. The results from these calculations are shown below in the respective sections.

3.3.2. NMP processed

The challenging part of interpreting the mass spectra in Fig. 7 is determining a reasonable value for the molecular ion. For example, using the 315-Da single-ion chromatogram (Fig. 6) and performing a correlation analysis showed that there were two candidates for the

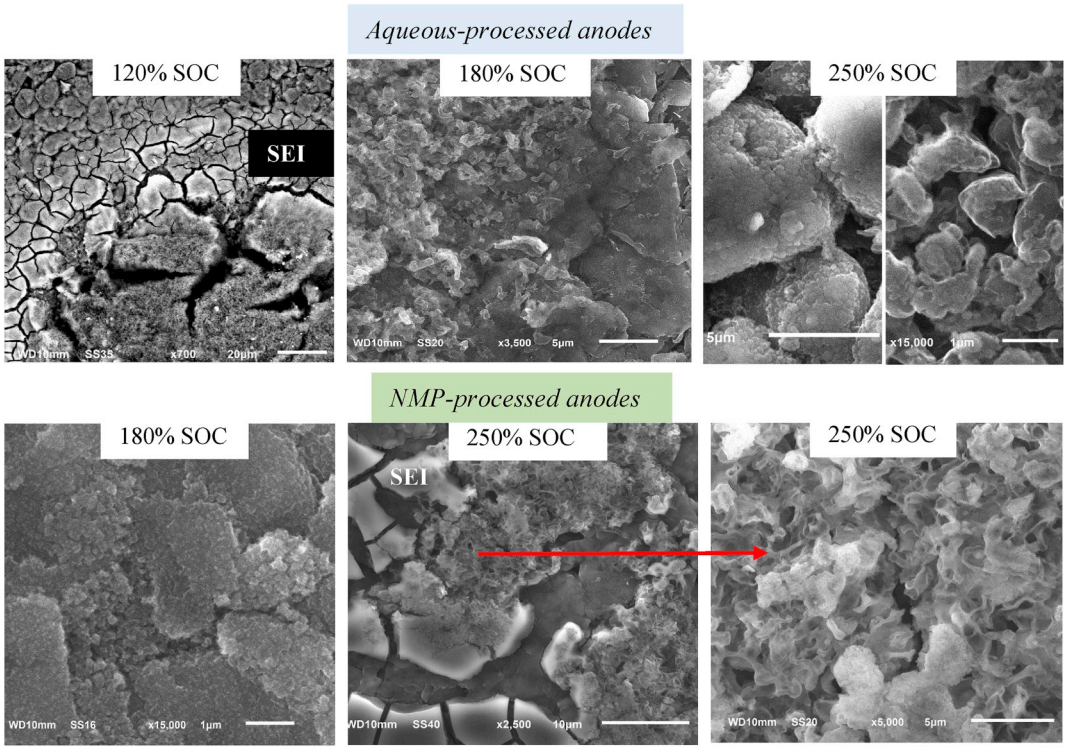

Fig. 4. Anode surfaces showing microstructural changes with increasing SOC. The arrow points to a region of growing dendrites.

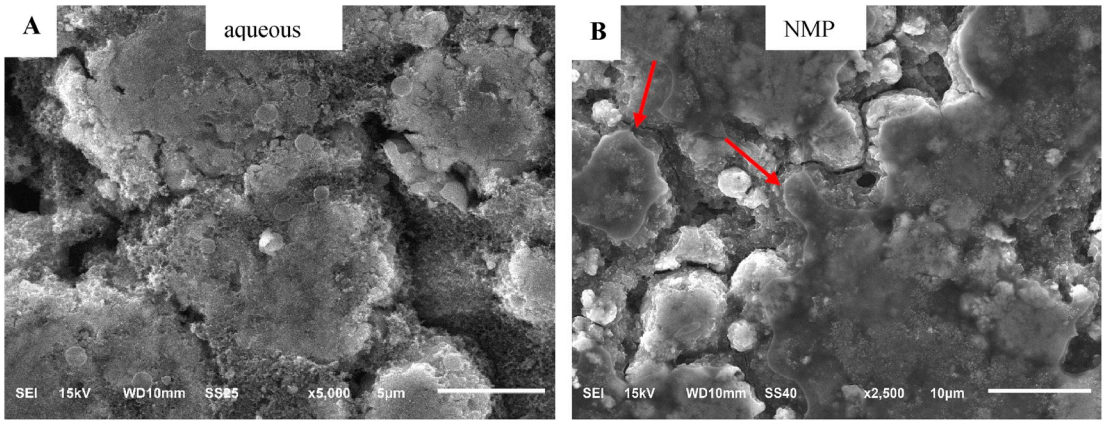

Fig. 5. (A) Aqueous-processed cathode surface showing round particles at 250% SOC, and (B) NMP-processed cathode surface showing encroachment of a cathode electrolyte interphase film on the surface at 250% SOC.

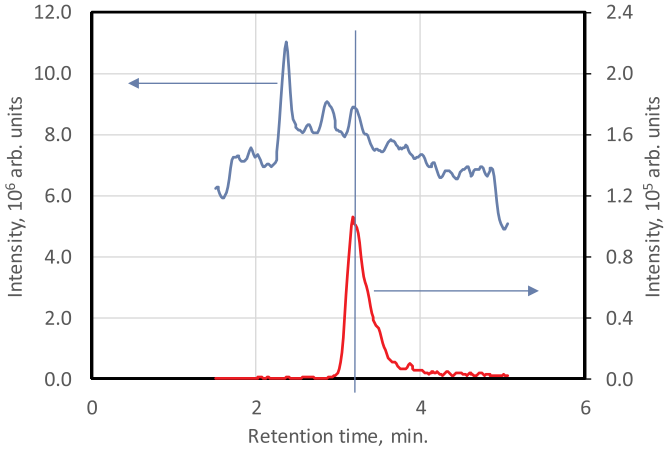

Fig. 6. Typical result of examining single-ion chromatograms. This example used the data from the 160% SOC cell (aqueous processed). The top curve is from the total-ion chromatogram, and the bottom, the single-ion chromatogram is for m/e = 315. The vertical blue line was added to aid the eye and to show the alignment of the peak in the bottom curve with a peak in the top curve. (For interpretation of the references to color in this figure legend, the reader is referred to the Web version of this article.)

molecular ion, 607 and 541 Da. The values of Pearson's *r* were close, 0.91 and 0.88, respectively. However, when the number of carbon atoms were calculated from the area ratio of the (*m*+1) to *m* peaks, only those values from the 607 peak made chemical sense (see Table 2). The values from the 541-Da peak ranged from 0.3 to ~56.

The results of determining reasonable values for the molecular ion are given in Table 2, along with proposed formulae for them and the calculated molecular weights for the proposed species.

If one compares the theoretical spectra (Fig. 7d–f) with the experimental ones in the molecular ion region, the theoretical positions of the *m*, (*m*+1) and (*m*+2) ions align well. The maximum error here is 0.3 Da. The intensities of the peaks in the experimental spectra appear to be different from those in the theoretical one, possibly due to reactions from collisions within the mass spectrometer [17].

Plotting the relative areas of the *m* peaks for the four species shown in Table 2 produces the graph shown in the top part of Fig. 8. From this plot, C is present in all samples. It starts as the only compound detected; compounds A, B, and D appear at higher states of charge, apparently at the expense of compound C. At states of charge greater than 140%, A decreases and, eventually, vanishes. It is interesting to note that D keeps increasing with percent SOC, becoming the dominant species found.

The area ratios of the *m* and (*m*+1) peaks were used to estimate the number of carbons in A, B, C, and D. The average values and standard deviations (1σ) are given in Table 2. Proposed formulae and molecular structures were constructed based on these values and expected electrolyte fragments, such as OCH_3, OCH_2CH_2O, H, PO_4, and $F_xP(=O)O_{3-x}$, using the principles outlined in Sahore et al. [18]. The proposed, empirical formulae are shown in Table 3 along with their calculated molecular weights, if one limits the number of phosphorus atoms in the compound to 3. Formulae for A, C, and D were found within one standard deviation from the average number of carbons. However, the proposed formula for D shown in Table 3 was not; the proposed formula for this compound was found within two standard deviations from the average value.

3.3.3. *Aqueous processed*

The plots of total ion count versus retention time for the anode extracts are shown in Fig. S2. Analysis of these data showed that there were two species that were common to all. One had a retention time of 2.81 min, and the other, 3.18 min. We found that two single-ion chromatograms corresponded to peaks at these retention times, 453 and 467 Da, respectively. The calculated mass spectra are shown in Fig. 7i and j.

We assumed that the species that gave rise to the 453- and 467-Da single-ion chromatograms were organic. Hence, the ratio of the areas of the (*m*+1) and *m* peaks can yield information regarding the number of carbons in the compound by comparing these area ratios to the ratio of naturally occurring ^{13}C–^{12}C. Based on this calculation, the average number of carbon atoms in the 453-Da compound was 13.8 ± 3.1.

Calculating the number of carbons in the 467-Da compound was a bit problematic. The area ratios of most led to between 9 and 13 carbon atoms, except for the value calculated from the 160% SOC. Here, it was ~33 carbon atoms. It is possible that the (*m*+1) peak contained an artifact, making it appear larger than expected. Omitting the spurious peak area yielded an average value of 11.0 ± 1.5 carbon atoms.

The proposed formulae in Table 4 and proposed molecules in Table 5 were constructed using principles that were described earlier [18]. These formulae and molecules were built from electrolyte degradation fragments, such as $–OCH_2CH_2O-$, and $LiPF_6$ decomposition products. Carbon–carbon double bonds were not proposed unless there was no other way to obtain a reasonable molecule with the combination of molecular weight and desired number of carbon atoms. These results are shown in Table 4. The theoretical mass spectra in the molecular ion region were calculated to add credence these results and are shown as Fig. 7k and l.

Visually comparing the plots in Fig. 7k and l reveals that the experimental and theoretical data agree well. There was a difference of 0.1 Da between respective molecular ion peaks in both plots. Proposed structural formulae (see Table 5) corresponding to these compounds were constructed using the principles alluded to above.

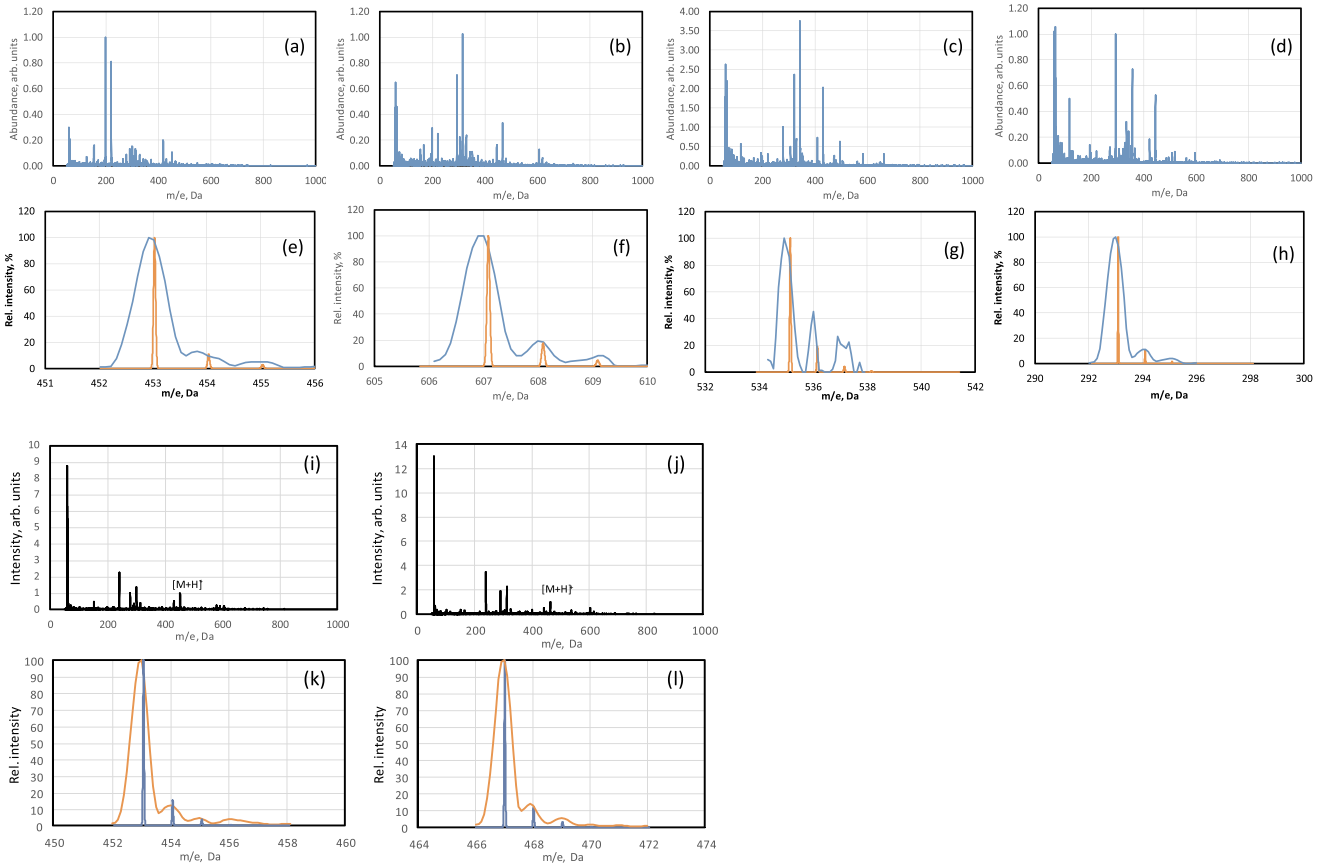

Fig. 7. (A)–(d) and (i)–(j): Calculated mass spectra for compounds A–D (NMP) and E–F (aqueous), using the data shown in Figs. S1 and S2, respectively, and single-ion chromatograms. (e)–(h) and (k)–(l): Comparison of the respective theoretical distribution in the molecular ion region with that experimentally observed. The orange curve represents the calculated data, and the blue, experimental. (For interpretation of the references to color in this figure legend, the reader is referred to the Web version of this article.)

Table 2
Results from calculations using data given in Fig. S1.

Label	Retention time (min)	Molecular ion (Da)	Number of carbon atoms (1σ)	Proposed formula[a]	Calc. Formula weight (g mol^{-1})
A	2.86	453	7.77 (0.96)	$[C_9H_{21}F_2O_{12}P_3]H^+$	453.18
B	3.15	607	11.39 (2.11)	$[C_{15}H_{33}F_2O_{15}P_3]Na^+$	607.32
C	4.85	535	16.66 (1.63)	$[C_{16}H_{34}F_2O_{13}P_2]H^+$	535.39
D	6.16	293	9.26 (0.46)	$[C_9H_{19}F_2O_6P]H^+$	293.22

[a] The sodium came from Na_2CO_3 used in the experimental procedure.

The relative areas of the molecular ion peaks were plotted as a function of percent SOC, as shown in Fig. 8. The 453-Da compound appears to be the major component at low percent SOCs. As the percent SOC increases, the relative amount of the 467-Da compound increases. At about 140% SOC, the two compounds appear to reach a steady state at about 50% each.

4. Discussion

The impact of the binder on the found organics (Tables 2–5) was far-reaching. Not only did the binder affect the number of constituents observed, it also affected their composition. With the NMP-soluble pVdF binder, four species were identified, and, with the water-soluble CMC/SBR binder, only two were found that tracked the extent of overcharge. One plausible reason could be the change in binder coverage, affecting the surface composition/properties of the anodes. It was demonstrated that the water-soluble binder displayed much higher coverage of the graphite anode than pVdF [19]. Thus, the anode surface is more uniform in the aqueous processed one and the SEI is less diverse (i.e., fewer compounds).

Inspecting the data in Tables 2 and 4 showed that there two compounds displaying molecular ions at 453 Da. In the CMC/SBR binder case, the compound was found to contain 13 carbon atoms in its empirical formula. On the other hand, that in the pVdF binder case contained only nine. Both species were thought to contain phosphate groups, but the former contained fewer. In addition, the compounds in the former case displayed more flexibility in terms of structural motifs: both phosphates and fluorophosphates were present. In the latter, only fluorophosphates were proposed. Thus, the binder may have influenced the chemistry of compounds in the SEI layer.

Indeed, the proposed compounds in Tables 3 and 5 indicate that the extent of polymerization of OCH_2CH_2O groups also appears to be sensitive to the binder. In the NMP-soluble case, compounds C and D have more OCH_2CH_2O groups in series (4 and 6, respectively) than A (1), B (1), E (3 and 2), and F (1 and 2). Compounds C and D are also more abundant than A and B, which may imply the polymerization is more

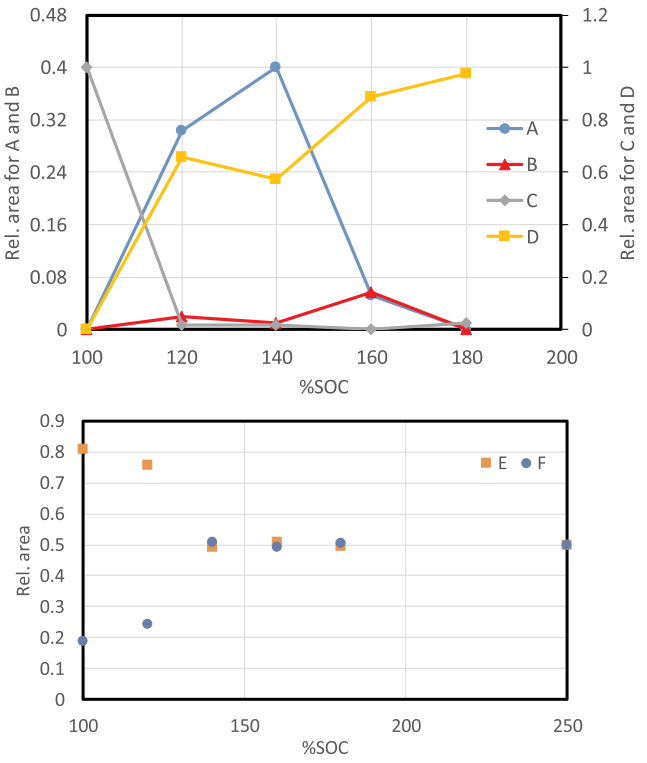

Fig. 8. Relative area of peaks vs. %SOC for materials extracted from the anodes.

Table 3
Proposed structural formulae based on the mass spectra results from the NMP-processed cells.

Label	Proposed structural formula
A	$[F_2P(=O)OCH_2CH_2OP(=O)(OCH_2CH_2OH)OCH_2CH_2OP(=O)(OCH_2CH_2OH)OCH_3]H^+$
B	$[F_2P(=O)OCH_2CH_2OP(=O)(OCH_2CH_2OCH_3)OCH_2CH_2OP(=O)(OCH_2CH_2OH)\text{-}(OCH_2CH_2)_3OH]Na^+$
C	$[F_2P(=O)OCH_2CH_2OP(=O)(OCH_2CH_2OH)(OCH_2CH_2)_6OH]H^+$
D	$[F_2P(=O)O(CH_2CH_2O)_4CH_3]H^+$

Table 4
Proposed formulae and calculated formula weights for the two compounds observed from the aqueous processed cells.

Compound	Found m/e (Da)	Proposed formula	Calculated formula weight (g mol^{-1})
E	453	$[C_{13}H_{28}O_{13}P_2]H^+$	453.3
F	467	$[C_{10}H_{23}O_{12}P_3F_2]H^+$	467.0

Table 5
Proposed molecular structures for the compounds discussed above. The compounds are given in the unprotonated state.

Compound	Proposed structural formula
E	$CH_3OP(=O)(OH)OCH_2CH_2OP(=O)(OCH\overline{=}CHOCH_2CH_2OH)(OCH\overline{=}CHOCH_2CH_2OCH_2CH_2OH)$
F	$F_2P(=O)OCH_2CH_2OP(=O)(OCH_3)OCH_2CH_2OP(=O)(OCH_3)OCH_2CH_2OCH_2CH_2OH$

favorable on the NMP-processed anode than on the aqueous-processed anode. Together, these observations also indicate that the interaction between the binder and the anode may be important in determining the composition of the SEI layer on the anode. One possible reason for this is that the NMP-soluble, pVdF binder is relatively nonpolar when compared to the water-soluble, CMC/SBR.

The nature of the binder layer on the anode may also affect the rate of lithium/lithium ions diffusing through it. If there were a greater prevalence of "lithium" in one case, then one would expect more free radicals, leading to, possibly, a greater extent of polymerization. This may explain the difference in chain lengths seen in the compounds mentioned above.

The above description may not be the complete story of how the SEI layer is formed. From the standpoint of logic, it is not unreasonable to consider that materials formed at the positive during charging may also migrate to the negative, forming part of the SEI layer.

Another possibility is that species formed at the cathode diffuse at different rates through the binder coating. The net effect would be that some species would be more prevalent at the anode for further reaction.

5. Conclusions

The effects of binder on the overcharging of LFP/graphite cells were investigated in small pouch cells and systematically charged to 100, 120, 140, 160, 180, and 250% SOC. The cells were then discharged to 3.0 V at room temperature before being disassembled for postmortem analysis.

Microstructural differences associated with increasing SOC were seen on the anode surfaces. Lithium deposition occurred sooner on the aqueous-processed anodes. Dendrites were observed at 120% SOC, whereas the NMP-processed anode consisted mainly of graphite particles that became progressively covered with particles with increasing percent SOC. Dendrites were not seen until 250% SOC. The aqueous-processed cathode surface was covered with small, round, flat particles that coalesced with increasing SOC. The NMP-processed cathode surface was covered in an amorphous film, or cathode electrolyte interphase layer, that gradually encroached on the surface with increasing SOC.

In NMP-soluble-binder case, four organic compounds on the anode surface were found to show a dependence on SOC. On the other hand, only two displayed a similar dependency in the water-soluble-binder case. The nature of the binder changed the number and composition of the species found at the anode.

Declaration of competing interest

The authors declare that they have no known competing financial interests or personal relationships that could have appeared to influence the work reported in this paper.

Acknowledgements

The authors thank Dr. Christopher S. Johnson (Argonne) and Dr. Ritu Sahore (ORNL) for fruitful discussions. We gratefully acknowledge support from the U.S. Department of Energy (DOE), Vehicle Technologies Office. Argonne National Laboratory is operated for DOE Office of Science by UChicago Argonne, LLC, under contract number DE-AC02-06CH11357.

The work at ORNL, managed by UT Battelle, LLC, for the DOE under contract DE-AC05-00OR22725, was sponsored by the Office of Energy Efficiency and Renewable Energy (EERE), Vehicle Technologies Office, Applied Battery Research.

Sandia National Laboratories is a multi-mission laboratory managed and operated by National Technology and Engineering Solutions of Sandia, LLC, a wholly owned subsidiary of Honeywell International, Inc., for the DOE's National Nuclear Security Administration (NNSA) under contract DE-NA0003525.

Appendix A. Supplementary data

Supplementary data to this article can be found online at https://doi.org/10.1016/j.jpowsour.2019.227595.

References

[1] K.A. Narayana, M.D. Casselman, C.F. Elliott, S. Ergun, S.R. Parkin, C. Risko, S. A. Odom, ChemPhysChem 16 (2015) 1179–1189.
[2] B. Wang, T.J. Richardson, G. Chen, Phys. Chem. Chem. Phys. 15 (2013) 6849–68555.
[3] J.-W. Wen, D.-W. Zhang, C.-H. Chen, C.-X. Ding, Y. Yu, J. Maier, J. Power Sources 264 (2014) 155–160.
[4] N. Dietz Rago, J. Bareño, J. Li, D.L. Wood III, L.A. Steele, J. Lamb, S. Spangler, C. Grosso, K. Fenton, I. Bloom, J. Power Sources 385 (2018) 145–155, https://doi.org/10.1016/j.jpowsour.2018.01.009.
[5] I. Bloom, J. Bareño, N. Dietz Rago, F. Dogan, D.G. Graczyk, Y. Tsai, S.R. Naik, S.-D. Han, E. Lee, Z. Du, Y. Sheng, J. Li, D.L. Wood III, L.A. Steele, J. Lamb, S. Spangler, C. Grosso, K.R. Fenton, J. Power Sources 385 (2018) 156–164, https://doi.org/10.1016/j.jpowsour.2017.12.015.
[6] J. Bareño, N. Dietz Rago, F. Dogan Key, D. Graczyk, Y. Tsai, S. Naik, S.-D. Han, E. Lee, Z. Du, Y. Sheng, J. Li, D. Wood, L.A. Steele, J. Lamb, S. Spangler, C. Grosso, K. Fenton, I. Bloom, J. Power Sources 385 (2018) 165–171, https://doi.org/10.1016/j.jpowsour.2017.12.061.
[7] W. Golukov, S. Scheikl, R. Planteu, G. Voitic, H. Wiltsche, C. Stangl, G. Fauler, A. Thalera, V. Hacker, RSC Adv. 5 (2015) 57171–57186.
[8] J. Lamb, C.J. Orendorff, K. Amine, G. Krumdick, Z. Zhang, L. Zhang, A.S. Gozdz, J. Power Sources 247 (2014) 1011–1017.
[9] F. Xu, H. He, Y. Liu, C. Dun, Y. Ren, Q. Liu, M. Wang, J. Xie, J. Electrochem. Soc. 159 (2012) A678–A687.
[10] F. Larsson, B.-E. Mellander, J. Electrochem. Soc. 161 (2014) A1611–A1617.
[11] Y. Liu, J. Xie, J. Electrochem. Soc. 162 (2015) A2208–A2217.
[12] J. Li, C. Daniel, S.J. An, D. Wood, MRS Adv. 1 (2016) 1029–1035.
[13] J. Li, C. Rulison, J. Kiggans, C. Daniel, D.L. Wood III, J. Electrochem. Soc. 159 (2012) A1152–A1157.
[14] J.Y. Howe, L.A. Boatner, J.A. Kolopus, L.R. Walker, C. Liang, N.J. Dudney, C. R. Schaich, J. Mater. Sci. 47 (3) (2012) 1572–1577.
[15] E.R. Malinowski, Factor Analysis in Chemistry, third ed., John Wiley and Sons, Inc., New York, 2002.
[16] https://en.wikipedia.org/wiki/Pearson_correlation_coefficient#For_a_sample.
[17] http://ww2.chemistry.gatech.edu/~kb12/3380/ms.pdf.
[18] R. Sahore, F. Dogan, I.D. Bloom, Chem. Mater. 31 (2019) 2884–2891.
[19] M. Wood, J. Li, R.E. Ruther, Z. Du, E.C. Self, H.M. Meyer III, C. Daniel, I. Belharouak, D.L. Wood III, Energy Storage Mater. 24 (2020) 188–197, https://doi.org/10.1016/j.ensm.2019.08.020.